Since January 2020 Elsevier has created a COVID-19 resource centre with free information in English and Mandarin on the novel coronavirus COVID-19. The COVID-19 resource centre is hosted on Elsevier Connect, the company's public news and information website.

Biosensors and Bioelectronics 215 (2022) 114563

Contents lists available at ScienceDirect

Biosensors and Bioelectronics

journal homepage: www.elsevier.com/locate/bios

Bipolar silica nanochannel array confined electrochemiluminescence for ultrasensitive detection of SARS-CoV-2 antibody

Jiawei Gong [a,1], Tongtong Zhang [b,1], Tao Luo [c], Xuan Luo [a], Fei Yan [a,*], Weizhong Tang [c,**], Jiyang Liu [a,***]

[a] Department of Chemistry, Key Laboratory of Surface & Interface Science of Polymer Materials of Zhejiang Province, Zhejiang Sci-Tech University, Hangzhou, 310018, China

[b] Department of Hepatobiliary and Pancreatic Surgery, The Center for Integrated Oncology and Precision Medicine, Affiliated Hangzhou First People's Hospital, Zhejiang University School of Medicine, Hangzhou, 310006, China

[c] Guangxi Medical University Cancer Hospital, Guangxi Medical University, 71 Hedi Road, Nanning, 530021, PR China

ARTICLE INFO

Keywords:
Silica nanochannel array
Bipolar surface charges
Solid-state electrochemiluminescence
Immunosensor
SARS-CoV-2 IgG antibody

ABSTRACT

Ultrasensitive, specific, and early identification of Coronavirus Disease (2019) (COVID-19) infection is critical to control virus spread and remains a global public health problem. Herein, we present a novel solid-state electrochemiluminescence (ECL) platform targeting severe acute respiratory syndrome coronavirus 2 (SARS-CoV-2) antibody with rapidity and ultrahigh sensitivity, in which a bipolar silica nanochannel array (bp-SNA) is fabricated on indium tin oxide (ITO) electrode for the first time to stably confine the ECL probe of tris(2,2′-bipyridyl) ruthenium ($Ru(bpy)_3^{2+}$) under dual electrostatic force. The bp-SNA consists of tightly packed bilayer silica nanochannel array (SNA) with asymmetric surface charges, namely an inner negatively charged SNA (n-SNA) and an outer positively charged SNA (p-SNA), serving as an "electrostatic lock" to enrich and stabilize the cationic $Ru(bpy)_3^{2+}$ probe without leakage from the electrode surface. The detection of SARS-CoV-2 IgG antibody could be realized *via* immobilization of SARS-CoV-2 spike protein on the utmost of $Ru(bpy)_3^{2+}$-confined solid-state ECL platform (Ru@bp-SNA). Upon the capture of target SARS-CoV-2 IgG by immune recognition, the formed immunocomplex will block the nanochannel, leading to the hindered diffusion of the co-reactant (tri-n-propylamine, TPrA) and further producing a decreased ECL signal. The developed solid-stated ECL immunosensor is able to determine SARS-CoV-2 IgG with a wide linear range (5 pg mL^{-1} to 1 μg mL^{-1}), a low limit-of-detection (2.9 pg mL^{-1}), and a short incubation time (30 min). Furthermore, accurate analysis of SARS-CoV-2 IgG in real serum samples is also obtained by the sensor.

1. Introduction

On-going coronavirus disease 2019 (COVID-19) pandemic caused by severe acute respiratory syndrome coronavirus 2 (SARS-CoV-2), poses an unprecedented threat to global public health, social behavior, economy, and everyone's life (Li et al., 2020; Wang et al., 2020). So far, it has brought out over 200 million infected cases with over 4 million deaths according to the World Health Organization (2021). In addition, the recent novel coronavirus has raised renewed exponential spread of the whole world owing to the asymptomatic nature and rapid mutation of the genetic sequence. Therefore, early identification of COVID-19 based on fast and effective diagnostic tests still represents one of the cornerstones to prevent or slow down the rapid spread of SARS-CoV-2 virus by presymptomatic and asymptomatic individuals. Real-time reverse transcription-polymerase chain (RT-PCR) reaction considered as the gold standard method for diagnosing COVID-19 but often requires a longer time to obtain results and the results may be false-negative owing to the low viral load in the infected persons (Woloshin et al., 2020; Xiao et al., 2020). Serological assays that focused on the detection of SARS-CoV-2 antibodies have the advantages of rapid speed, specificity

* Corresponding author.
** Corresponding author.
*** ***Corresponding author.
E-mail addresses: yanfei@zstu.edu.cn, feifei19881203@126.com (F. Yan), tangweizhong@gxmu.edu.cn (W. Tang), liujy@zstu.edu.cn (J. Liu).
[1] These two authors contributed equally.

https://doi.org/10.1016/j.bios.2022.114563
Received 7 May 2022; Accepted 8 July 2022
Available online 14 July 2022

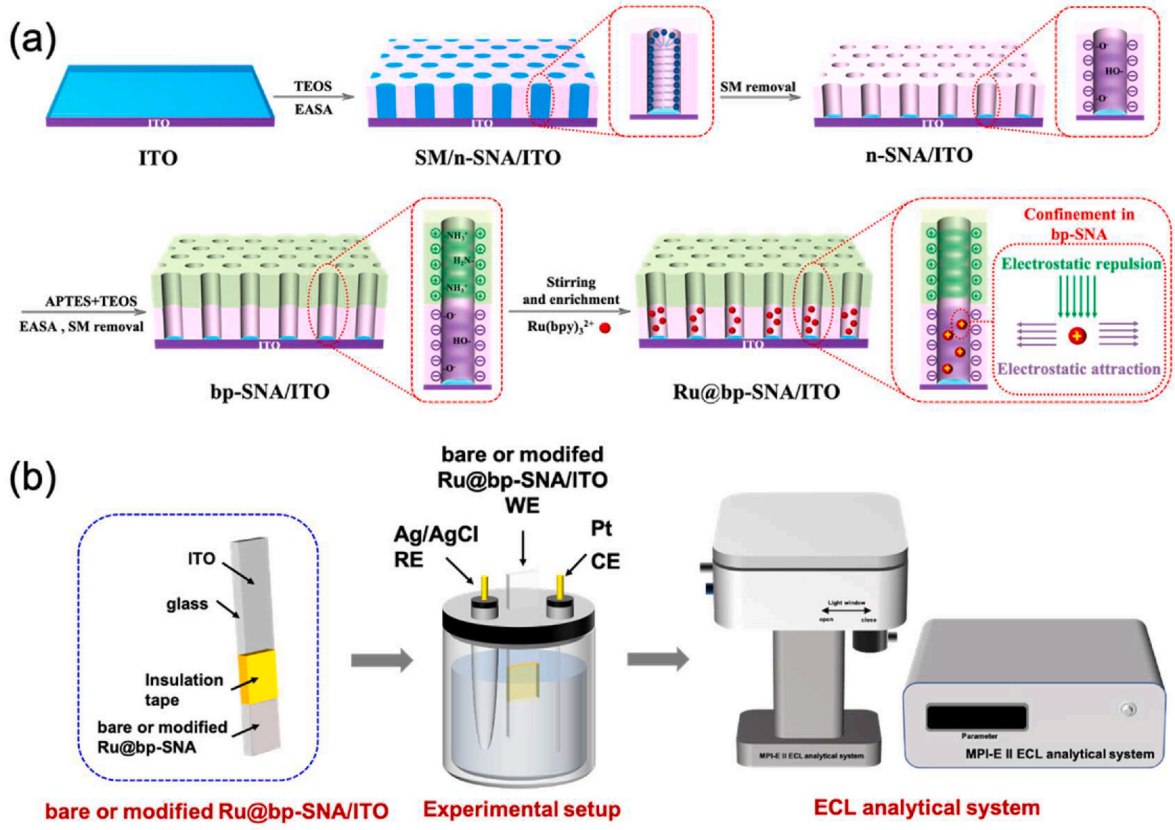

Fig. 1. Schematic illustration for the preparation of the Ru@bp-SNA/ITO electrode (a) and ECL testing setup (b).

and easy operation, and thus could be served as a great complement diagnostic tool to RT-PCR (Lee et al., 2020; Petherick, 2020). Moreover, as the COVID-19 vaccines are deployed worldwide, detection of SARS-CoV-2 antibodies for vaccinated persons is vital for monitoring the dynamic humoral response and further evaluating the effectiveness of a vaccine (Krammer and Simon, 2020). Developing rapid, reliable and ultrasensitive platforms for quantitative detection of SARS-CoV-2 antibodies are highly desirable. At present, commercial methods for the SARS-CoV-2 antibodies detection include enzyme linked immunosorbent assay (ELISA) and gold immunochromatography assay. ELISA requires multiple operation steps (e.g. sample dilution and plate washing), lengthy incubation time (3–4 h) and experimental apparatus, which should be performed by professional persons in a laboratory. Gold immunochromatography assay involves multiple labeling steps of antibodies and the obtained results are semiquantitative. Electrochemical technique with high sensitivity and portability is a well-suited method for SARS-CoV-2 antibodies detection but still less studied (Ali et al., 2021; Rashed et al., 2021; Torrente-Rodriguez et al., 2020; Yakoh et al., 2021) and especially electrochemiluminescence (ECL) has not been reported previously, to the best of our knowledge.

ECL has emerged as a powerful analytical tool for immunoassays due to its zero background, high sensitivity, and easy integration with miniaturized devices (Hu and Xu, 2010; Richter, 2004). At present, tris (2,2′-bipyridyl)ruthenium(II) ($Ru(bpy)_3^{2+}$) and its derivatives or $Ru(bpy)_3^{2+}$ loaded nanomaterials with high efficiencies and stable signal can serve as the excellent ECL luminophores, which have been widely applied in commercial ECL systems (Guo et al., 2018; Miao, 2008). ECL of $Ru(bpy)_3^{2+}$-based luminophores could be realized by two categories. One is to directly utilize the luminophores in solutions, namely solution-phase ECL, and the other is to immobilize them on the electrode surface, namely solid-state ECL. Due to the inherent regeneration in the process of ECL reaction, $Ru(bpy)_3^{2+}$-based luminophores are very suitable for the construction of solid-state ECL. Moreover, in comparison with solution-phase ECL, solid-state ECL has manifested themselves to be a useful and alternative approach owing to the easy operation, low consumption of expensive luminophores and samples, low-cost and reusability (Wei and Wang, 2008). Until now, various techniques including Langmuir-Blodgett film (Bertoncello et al., 2007; Miller et al., 1991; Zhang and Bard, 1988), sol-gel entrapment (Collinson et al., 2000; Sykora and Meyer, 1999; Wang et al., 2001), layer-by-layer self--assembly (Guo et al., 2004), ion-exchange (Guo and Dong, 2004; Khramov and Collinson, 2000), and covalent binding (Wang et al., 2019; Wei et al., 2008), have been reported for the immobilization of Ru $(bpy)_3^{2+}$-based ECL luminophores on the surface of electrode. However, above methods often need complex operation and the obtained Ru $(bpy)_3^{2+}$-based ECL luminophores immobilized on the electrode surface are rather few and tend to penetrate away from the electrode surface into the solution during the test, significantly disturbing the sensitivity and durability of the sensors. Therefore, developing highly sensitive, stable and convenient solid-state ECL platforms with high loading of Ru $(bpy)_3^{2+}$-based luminophores to realize the standard of immunoassays, has important meanings.

Recently, Su group designed a nanocage array consisted of two layers of silica nanochannel array (SNA) with vertically ordered nanochannels and different pore diameters for physical trap of $Ru(bpy)_3^{2+}$ derivative, which successfully functioned as a solid state ECL sensor (Ding et al., 2020). This method relies on the nanospace-based confinement of two layers of SNA and $Ru(bpy)_3^{2+}$ derivatives with larger size are needed. Generally, such $Ru(bpy)_3^{2+}$ derivatives are acquired by using the chemical modification of $Ru(bpy)_3^{2+}$, resulting in the decreased water solubility and further reducing the loading amount on the electrode surface. Moreover, PMMA-assisted transfer method used in the fabrication process is tedious and time-consuming. In this work we fabricate a bipolar silica nanochannel array (bp-SNA) for the first time to build up a "electrostatic lock" for the stable confinement of $Ru(bpy)_3^{2+}$ and explore its performance in the field of solid-state ECL sensors. Such bp-SNA with

asymmetric surface charges consists of an inner negatively charged SNA (n-SNA) layer and an outer positively charged SNA (p-SNA) layer and could be prepared by using very simple electrochemically assisted self-assembly (EASA) method. Due to the ultrasmall pore size of both two layers of SNA (within the Debye screening length), bp-SNA exerted a dual electrostatic force towards $Ru(bpy)_3^{2+}$, that is, $Ru(bpy)_3^{2+}$ electrostatically immobilized on the inner n-SNA layer was effectively locked in the film without leakage through the electrostatic repulsion by outer p-SNA, leading to the sensitive and stable ECL signal. As a proof of concept, SARS-CoV-2 IgG antibody was chosen as the target species by the construction of bp-SNA-based immuno-recognition interface. The results indicated that our designed solid-state ECL sensor was able to detect SARS-CoV-2 IgG with ultrahigh sensitivity and excellent stability, offering a universal ECL platform for more biomolecules (e. g. SARS-CoV-2 antigen) in clinical diagnosis.

2. Materials and Methods

2.1. Chemicals and instruments

Details of chemicals and instruments are presented in the supplementary information.

2.2. Preparation of n-SNA/ITO electrode

As reported previously (Goux et al., 2009; Walcarius et al., 2007), n-SNA was prepared on the bare ITO electrode (1 cm × 0.5 cm) by using the EASA method (Fig. 1a). Briefly, a mixture consisting of 0.1 M $NaNO_3$ aqueous solution (20 mL), ethanol (20 mL), TEOS (3.05 mL), and CTAB (4.35 mmol) was firstly prepared and its pH was adjusted to 2.6 by the addition of 1 M HCl aqueous solution. After being pre-hydrolyzed under stirring for 2.5 h, the silica-based precursor was obtained. Then the bare ITO electrode was immersed into the above solution and underwent a constant current density (−0.70 mA cm^{-2}) for 10 s. After being quickly rinsed with ultrapure water, aged at 120 °C overnight and removal of CTAB micelles from nanochannels with HCl-ethanol solution (0.1 M) under stirring for 5 min, SNA with negatively charged nanochannel walls supported on the ITO electrode was obtained, termed as n-SNA/ITO.

2.3. Preparation of bp-SNA/ITO and Ru@bp-SNA/ITO electrodes

bp-SNA/ITO electrode was fabricated using the EASA method (Goux et al., 2009; Walcarius et al., 2007) and subsequently electrostatic confinement of $Ru(bpy)_3^{2+}$ inside the nanochannels of bottom n-SNA layer, to obtain electrochemiluminescent Ru@bp-SNA/ITO electrode (Fig. 1a). According to the previous report (Etienne et al., 2009), addition of APTES directly into the precursor solution is able to grow SNA with positively charged nanochannels, designated as p-SNA, *via* co-condensation of amino groups covalently bonded to the silica nanochannel walls. Typically, the precursor solution contains ethanol (20 mL), CTAB (4.35 mmol), TEOS (2.732 mL) and APTES (0.318 mL) and $NaNO_3$ (20 mL, 0.1 M, pH = 2.6). Before the growth of p-SNA, the obtained precursor solution was pre-hydrolyzed under stirring at room temperature for 2.5 h. Then the n-SNA/ITO electrode was immersed into the precursor solution and applied a constant current density (−0.70 mA cm^{-2}) for 15 s. The resulting electrode was immediately taken out, rinsed by copious amount of water and aged at 120 °C overnight. bp-SNA/ITO electrode was achieved after removal of CTAB micelles from silica nanochannels. Then the obtained bp-SNA/ITO electrode was treated with 0.01 M PBS (pH = 7.4) containing 1 mM $Ru(bpy)_3^{2+}$ solution under stirring for 1 h, leading to the electrostatic trap of $Ru(bpy)_3^{2+}$ inside the nanochannels of bottom n-SNA and eventually producing Ru@bp-SNA/ITO electrode. In comparison, n-SNA/ITO electrode was also used to confine $Ru(bpy)_3^{2+}$, termed as Ru@n-SNA/ITO.

2.4. Fabrication of the immunosensor

Owing to the presence of amino groups on p-SNA, glutaraldehyde (GA) was chosen as the bifunctional linker for covalent immobilization

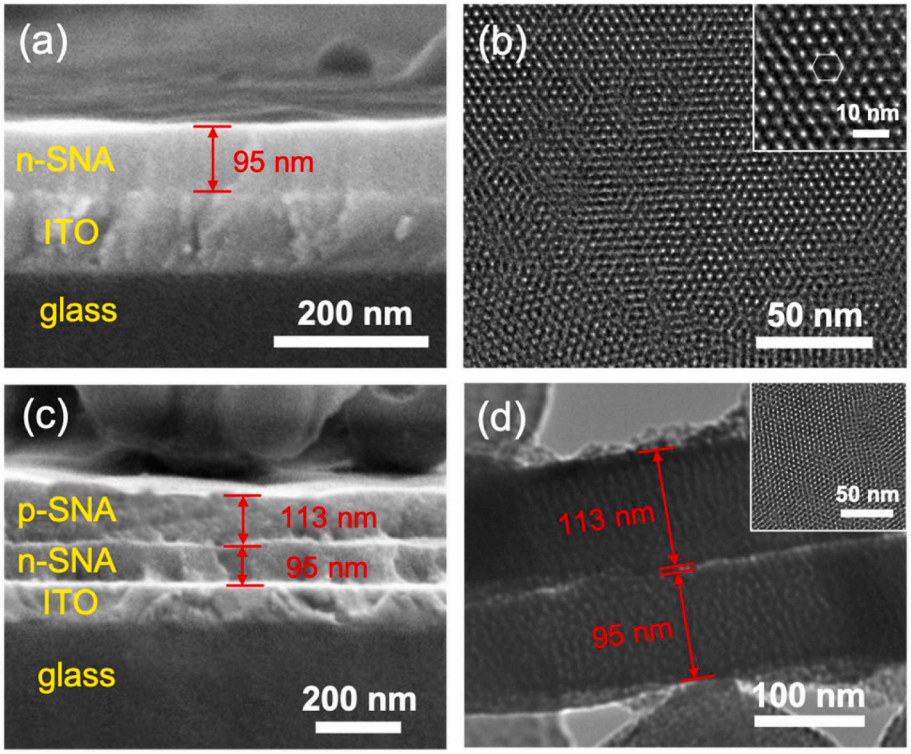

Fig. 2. (a) Cross-sectional SEM image of n-SNA/ITO. (b) Top-view TEM image of n-SNA at different magnifications. Cross-sectional SEM (c) and TEM (d) images of bp-SNA/ITO. Insets in (b) and (d) are the top-view TEM image of n-SNA and bp-SNA respectively.

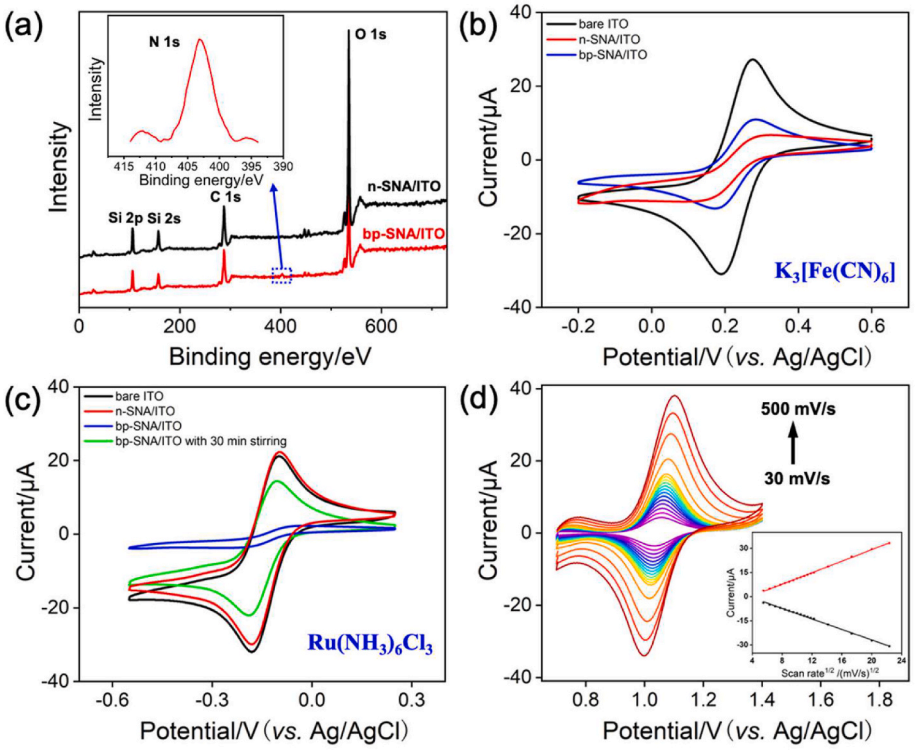

Fig. 3. (a) XPS profiles of the n-SNA/ITO and bp-SNA/ITO electrodes. Inset is high-resolution N1s spectrum of the bp-SNA/ITO. (b–c) CV curves of 0.5 mM $K_3[Fe(CN)_6]$ or (c) $Ru(NH_3)_6Cl_3$ on different electrodes at a scan rate of 50 mV/s. The supporting electrolyte is 0.05 M KHP. (d) CV curves of the Ru@bp-SNA/ITO electrode in 0.01 M PBS (pH 7.4) at various scan rates. Inset is the dependence of anodic and cathodic peak currents on the square root of scan rate.

of the recognitive ligands. Firstly, Ru@bp-SNA/ITO electrode was immersed into a GA solution (5%, in 0.01 M PBS, pH 7.4) under 37 °C for 1 h in dark (Mi et al., 2020). After unlinked GA was washed off, the resulting electrode was immersed in a SA solution (500 ng mL^{-1}, in 0.01 M PBS, pH 7.4) and reacted at 37 °C for 1 h. The obtained electrode was termed as SA/Ru@bp-SNA/ITO. Then, biotin-labeled SARS-CoV-2 antigen (Bio-Ag, 40 μL, 2 μg mL^{-1}) was dropped onto the surface of SA/Ru@bp-SNA/ITO electrode and incubated for 1 h at 37 °C. After loosely bounded Bio-Ag was washed off, the obtained electrode was treated with BSA (1 mg mL^{-1} in 0.01 M PBS, pH 7.4) to block non-specific binding sites, eventually producing the Bio-Ag/SA/Ru@bp-SNA/ITO electrode, and stored at 4 °C prior to use.

2.5. Detection of SARS-CoV-2 IgG

To detect SARS-CoV-2 IgG, Bio-Ag/SA/Ru@bp-SNA/ITO sensor was incubated with different concentrations of SARS-CoV-2 IgG for 0.5 h at room temperature. The ECL intensities after the binding of SARS-CoV-2 IgG were measured. Serum (healthy man) was diluted by a factor of 50 using PBS (0.01 M, pH 7.4) for real sample analysis. A defined amount of SARS-CoV-2 IgG was added into the diluted serum before ECL detection. As shown in Fig. 1b, Bio-Ag/SA/Ru@bp-SNA/ITO, Ag/AgCl electrode (saturated with KCl solution) and platinum wire were chosen as the working electrode, reference electrode and counter electrode, respectively. Continuous scanning potential is from 0 V to 1.5 V and the PMT voltage is biased at 450 V.

3. Results and discussion

3.1. Convenient preparation of bp-SNA/ITO electrode

Fig. 1a illustrates the preparation of ITO electrode modified with bp-SNA consisting of bilayer SNA with asymmetric surface charges, namely an inner negatively charged SNA (n-SNA) layer and an outer positively charged SNA (p-SNA) layer. n-SNA was first grown on the ITO electrode using EASA method (Goux et al., 2009) to obtain the n-SNA/ITO. Due to the deprotonation of silanol groups, the surface of obtained pristine SNA is negatively charged, after removal of CTAB surfactant micelles (SM) from silica nanochannels. Subsequently, p-SNA was overlaid onto the n-SNA/ITO using EASA method (Etienne et al., 2009; Giordano et al., 2017). Introduction of APTES into the silica-based precursor produces amino groups on the silica walls during the co-condensation process, conferring the positively charged channel surface. Owing to the Si–O chemical bonding at the interface between n-SNA and p-SNA, the prepared bilayer SNA with asymmetric surface charges, designated as the bp-SNA/ITO electrode, is rather stable. Such bipolar nanochannel array structure was applied to confine $Ru(bpy)_3^{2+}$ ECL luminophores *via* the prominent electrostatic effect, to finally obtain Ru@bp-SNA/ITO electrode. $Ru(bpy)_3^{2+}$ trapped into the nanochannels of n-SNA experienced a dual electrostatic force in confined nanospace, namely electrostatic attraction from inner n-SNA layer and electrostatic repulsion from outer p-SNA layer, giving rise to the sensitive and stable ECL signal.

3.2. Characterizations of bp-SNA/ITO and Ru@bp-SNA/ITO electrodes

The morphology and structure of n-SNA/ITO and bp-SNA/ITO were first characterized by scanning electron microscopy (SEM) and transmission electron microscopy (TEM). As shown in the cross-sectional SEM in Fig. 2a, n-SNA with homogeneous and flat thickness (~95 ± 1 nm, n = 3) is grown on ITO surface. Top-view TEM images of n-SNA displayed in Fig. 2b reveal the uniform and hexagonally packed nanochannels without the fractures over a large domain. The pore diameter of n-SNA is 2.3 ± 0.3 nm (n = 11). Fig. 2c shows the cross-sectional view of bp-SNA/ITO. Four layers from top to down can be obviously observed, corresponding to p-SNA (~113 ± 1 nm, n = 3), n-SNA, ITO and glass substrate, respectively. And the relative standard deviations (RSD) for the thickness of n-SNA and p-SNA from three independently prepared electrodes are within 2.2%. The cross-sectional TEM image

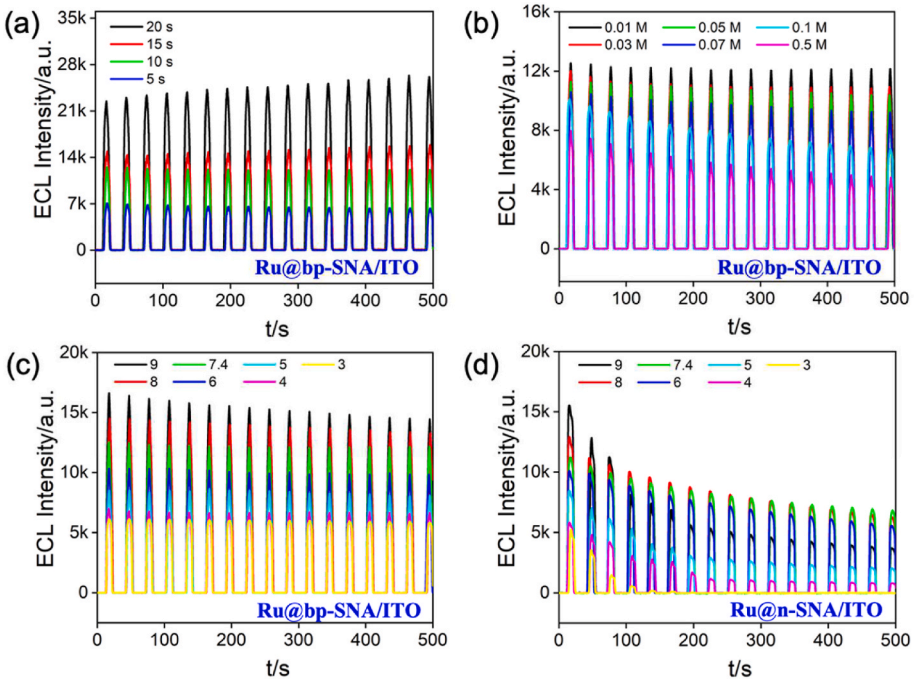

Fig. 4. Time-dependent ECL signals of the Ru@bp-SNA/ITO electrode for successive CV scans at different growth time of n-SNA (a), different concentrations (b) and pH (c) of supporting electrolyte. (d) Time-dependent ECL signals of the Ru@n-SNA/ITO electrode for successive CV scans at different pH. The concentration of the TPrA is 3 mM.

confirms the perpendicular nanochannels and double-layer structure of bp-SNA. (Fig. 2d). Their thickness of p-SNA and n-SNA captured in TEM are consistent with that obtained in SEM investigation. Note that the growth of outer p-SNA still remains the ordered nanochannel structure of whole bilayer SNA (inset in Fig. 2d).

In order to prove the presence of amino groups onto the channel walls of p-SNA layer, X-Ray photoelectron spectroscopy (XPS) characterization is employed. Fig. 3a compares the XPS spectra of n-SNA and bp-SNA. As seen, a characteristic peak of bp-SNA at 403 eV corresponding to the N 1s was observed, suggesting the successful growth of amino-functionalized SNA. The electrostatic permselectivity of bp-SNA/ITO electrode was investigated by Cyclic voltammetry (CV) using two charged electrochemical probes, namely anionic $Fe(CN)_6^{3-}$ and cationic $Ru(NH_3)_6^{3+}$. Fig. 3b and c compare CVs obtained from bare ITO, n-SNA/ITO and bp-SNA/ITO electrodes in 0.05 M KHP containing 0.5 mM $Fe(CN)_6^{3-}$ (b) or $Ru(NH_3)_6^{3+}$ (c). Note that electrical double layer (EDL) in the radial direction of nanochannels tends to overlap in this experimental condition. It can be found that n-SNA/ITO electrode arising from the deprotonation of silanol groups is permselective to cationic $Ru(NH_3)_6^{3+}$. After the formation of bp-SNA, the access of $Fe(CN)_6^{3-}$ ($Ru(NH_3)_6^{3+}$) through the nanochannels suffers from the synergistic effect of electrostatic attraction (repulsion) from outer p-SNA layer and electrostatic repulsion (attraction) from inner n-SNA layer. In comparison with the n-SNA/ITO, an increased current magnitude for $Fe(CN)_6^{3-}$and a much decreased one for $Ru(NH_3)_6^{3+}$ were observed at the bp-SNA/ITO, indicating surface charges of outer p-SNA layer have effect on the whole permselectivity of bp-SNA. However, $Ru(NH_3)_6^{3+}$ could break through the electrostatic resistance by the outer p-SNA layer and access to the underlying ITO electrode surface through the nanochannels of bp-SNA under stirring, eventually giving rise to the comparable electrical current compared to that of bare ITO (Fig. 3c). The results also suggest that stirring method could be used to confine cationic species into the inner layer of the bp-SNA. Fig. 3d gives the CV curves of Ru@bp-SNA/ITO electrode in 0.01 M PBS (pH 7.4) at different scan rates. When scan rates increase, both anodic and cathodic peak currents increase. And linear relationship between peak currents and square root of scan rate is observed, indicating a diffusion controlled electrochemical process and further proving the $Ru(bpy)_3^{2+}$ probe electrostatically trapped into the nanochannels of n-SNA is still diffusive. This nano-space confinement will make ECL luminophores on the electrode surface, which is expected to improve the efficiency of electrochemistry and ECL reaction.

3.3. *Optimization conditions for ECL signals obtained at the Ru@bp-SNA/ITO electrode*

Considering the bp-SNA with opposite surface charges, several experimental conditions should be investigated to obtain high ECL signals, such as the thickness of n-SNA, buffer ionic strength and pH. As the inner n-SNA layer determines the enrichment capability towards $Ru(bpy)_3^{2+}$, optimization of its thickness is especially important and its thickness could be easily controlled by adjusting the electrodeposition time in EASA method. We have prepared n-SNA layer using different electrodeposition time (5 s, 10 s, 15 s, and 20 s) and their corresponding thickness was estimated as 74 nm, 94 nm, 148 nm, 240 nm, respectively (Fig. 2a and Fig. S1). As shown in Fig. 4a, the ECL intensity of the Ru@bp-SNA/ITO electrode increases with increasing the thickness of n-SNA layer, which is probably attributed to the improved electrostatic adsorption capacity of long nanochannels. However, when the electrodeposition time exceeds 10 s, the relative standard deviation (RSD) for continuous ECL measurements ($n = 17$) increases (0.83% for 10 s and 5.06% for 20 s). This may be due to the reduced order of longer nanochannels. Thus, 10 s is chosen as the optimal electrodeposition time for the growth of n-SNA in the following study.

Ionic strength and pH of supporting electrolyte are related to the surface charge state of bp-SNA, finally regulating the permselectivity of the whole electrode material. Fig. 4b illustrates the seventeen consecutive ECL intensity curves of the Ru@bp-SNA/ITO electrode in various concentrations of PBS (pH 7.4). As revealed, upon increasing the concentration of supporting electrolyte, both ECL signal magnitude and stability of the Ru@bp-SNA/ITO electrode decrease, which is ascribed to the weak or disappeared EDL effect inside the silica nanochannel in the high concentration range. The maximal ECL intensity and the best

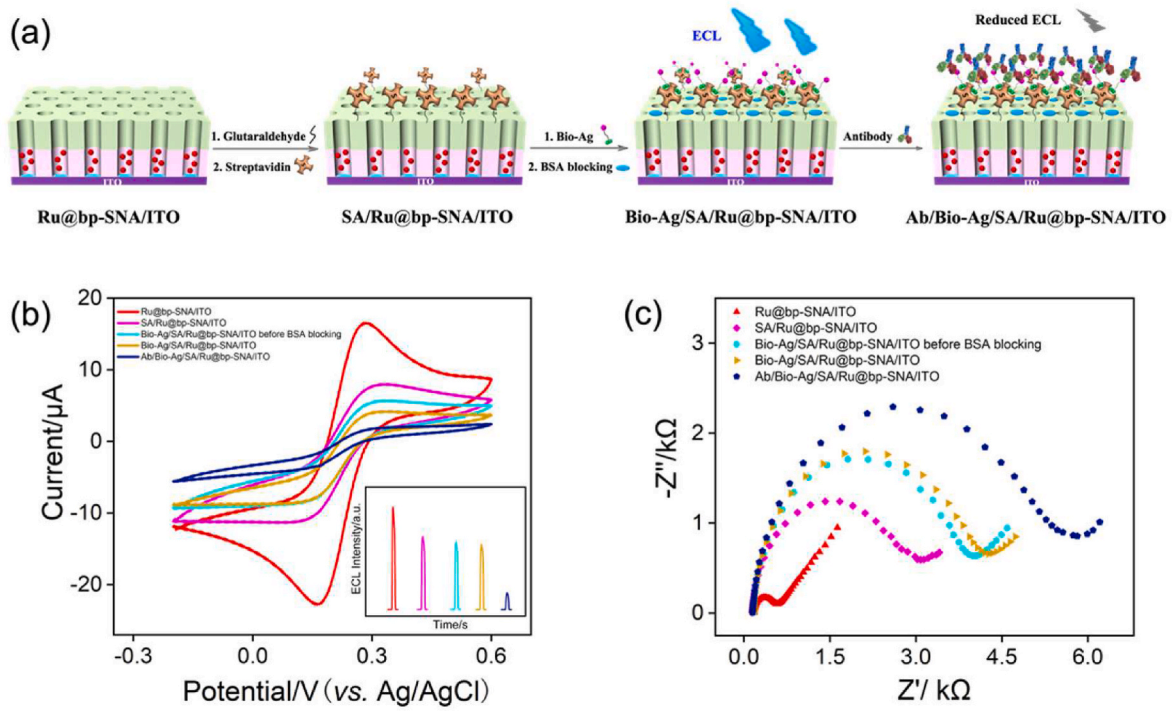

Fig. 5. (a) Schematic illustration for the fabrication of the label-free immunoassay for the ECL detection of SARS-CoV-2 IgG. CV (b) and EIS (c) curves on different electrodes in 0.05 M KHP containing 0.5 mM $K_3[Fe(CN)_6]$. The scan rate is 50 mV/s. Insets in (b) is the corresponding ECL curves.

stability (RSD~0.83%) is obtained at the concentration of 0.01 M. Note that the overlap of EDL occurs inside the silica nanochannels of bp-SNA and electrostatic effect towards $Ru(bpy)_3^{2+}$ becomes strong in this case. Fig. 4c shows the effect of pH on the ECL intensity of the Ru@bp-SNA/ITO electrode. As seen, increasing the pH value of PBS from 4 to 9 leads to a remarkably increased ECL intensity, mostly due to an increasing negatively charged surface charge of inner n-SNA layer. In addition, when pH varies from 4 to 7.4, the Ru@bp-SNA/ITO sensor has excellent ECL stability (RSD <2.09%). But reduced ECL stability is found after pH is over 7.4, which may be resulted from the declined positively charged surface charge of outer p-SNA layer (pK_a of propylamine~10.71). The long-term ECL signals of the Ru@n-SNA/ITO electrode at various pH of supporting electrolyte were comparatively studied and the results are shown in Fig. 4d. The magnitudes of ECL intensity obtained on an Ru@n-SNA/ITO are almost close to that on a Ru@bp-SNA/ITO at first scan. However, at the Ru@n-SNA/ITO electrode without outer p-SNA layer, the ECL intensities rapidly decay during consecutive measurements and only remain part of the initial values. It could be found that the RSD value (21.93%) obtained at the Ru@n-SNA/ITO electrode in the following test condition (pH = 7.4) is much higher than that of the Ru@bp-SNA/ITO (0.83%) electrode (Fig. S2). Especially, the ECL signal at a pH of 3 is nearly disappeared after the 7th measurement indicating the outer p-SNA can act as a protective layer to prevent the immobilized $Ru(bpy)_3^{2+}$ from diffusing to the bulk solution over prolonged use. Above results also confirm that this designed Ru@bp-SNA/ITO sensor is capable of preconcentrating and stably trapping the $Ru(bpy)_3^{2+}$ ECL luminophore inside the silica nanochannels *via* dual electrostatic force, finally resulting in a high and stable ECL signal. Given the excellent antifouling of pristine SNA, we believe this senor possesses relatively high stability and reproducibility in the direct analysis of complex real samples.

3.4. Fabrication of immunorecognitive interface on Ru@bp-SNA/ITO electrode

Taking SARS-CoV-2 IgG antibody (simplified as Ab in Fig. 5) as the target, recognitive species, biotin-labeled SARS-CoV-2 spike protein (Bio-Ag) as antigen was immobilized on the Ru@bp-SNA/ITO electrode based on the biotin-streptavidin (SA) binding reaction (Fig. 5a), involving two steps, namely modifying amino groups of bp-SNA with SA using bifunctional glutaraldehyde (GA) as crosslinker (designated as SA/Ru@bp-SNA/ITO) and subsequent binding Bio-Ag to SA/Ru@bp-SNA/ITO to construct the immunorecongnitive interface (designated as Bio-Ag/SA/Ru@bp-SNA/ITO). CV and electrochemical impedance spectroscopy (EIS) were employed to characterize the interface variation in the fabrication process of the Bio-Ag/SA/Ru@bp-SNA/ITO electrode using $Fe(CN)_6^{3-}$ as the redox probe. As shown in Fig. 5b, obvious decreased redox currents of $Fe(CN)_6^{3-}$ are found at the SA/Ru@bp-SNA/ITO electrode in comparison with Ru@bp-SNA/ITO, which is owing to the increased interface resistance produced by the non-conductive nature of proteins (SA). Similarly, the following immobilization of Bio-Ag and blocking with BSA further lead to the reduced redox signals of $Fe(CN)_6^{3-}$. After the Bio-Ag/SA/Ru@bp-SNA/ITO electrode was incubated with SARS-CoV-2 IgG, the magnitude of redox peak currents significantly decreases, proving that SARS-CoV-2 IgG could be specifically recognized by immobilized Bio-Ag and then antigen-antibody immunocomplex was formed. Variation of ECL signals on each step is in accordance with that of CV responses (inset of Fig. 5b). Fig. 5c displays the EIS plots of the Ru@bp-SNA/ITO, SA/Ru@bp-SNA/ITO, Bio-Ag/SA/Ru@bp-SNA/ITO with or without BSA blocking and Ab/Bio-Ag/SA/Ru@bp-SNA/ITO in 0.05 M KHP containing 0.5 mM $Fe(CN)_6^{3-}$. Apparently, the interfacial electron transfer resistances increase with the successive assembly, further confirming the successful immobilization process of immunosensing interface and the great potential for the SARS-CoV-2 IgG detection. Moreover, SARS-CoV-2 IgM with larger size could also be recognized by SARS-CoV-2 spike protein and display a higher sensitivity than SARS-CoV-2 IgG due to the more considerable hindrance toward the redox reaction (Yakoh et al., 2021). We believe that the present Bio-Ag/SA/Ru@bp-SNA/ITO sensor also possesses the same characteristics.

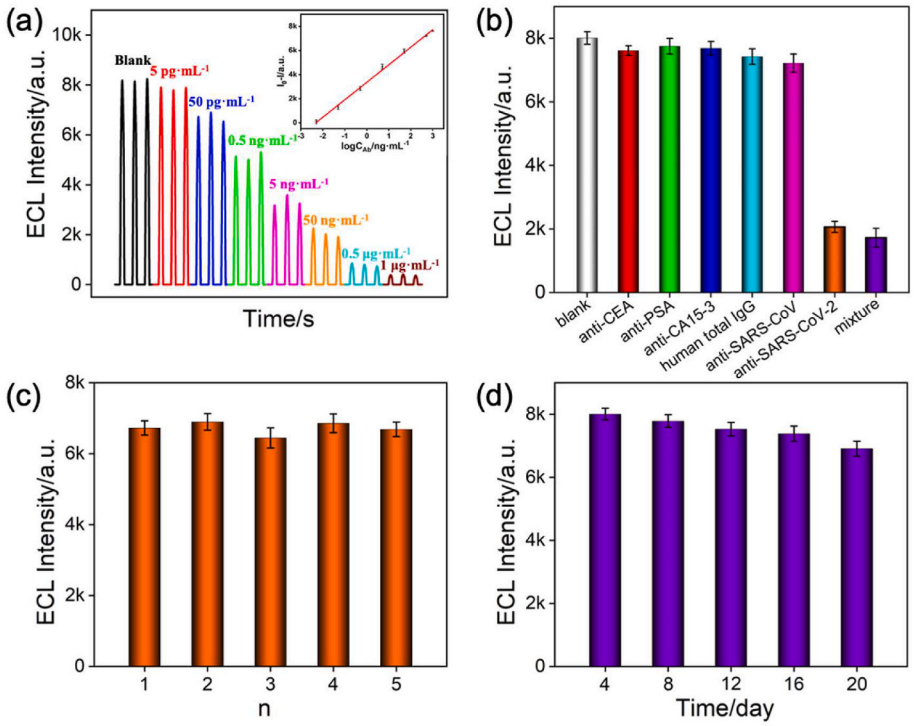

Fig. 6. (a) ECL responses of the immunosensor to different concentrations of SARS-CoV-2 IgG from 5 pg mL^{-1}, 50 pg mL^{-1}, 0.5 ng mL^{-1}, 5 ng mL^{-1}, 50 ng mL^{-1}, 0.5 μg mL^{-1} to 1 μg mL^{-1}. Inset is the corresponding calibration curve. (b) The specificity of the ECL immunosensor toward different antibodies. The concentration of anti-CEA, anti-PSA, anti-CA15-3, human total IgG and anti-SARS-CoV is 500 ng mL^{-1} and the concentration of SARS-CoV-2 IgG is 50 ng mL^{-1}. (c) The ECL intensity of five immunosensors prepared in parallel for the detection of 50 pg mL^{-1} SARS-CoV-2 IgG. (d) The ECL intensity of the immunosensor in the presence of 5 pg mL^{-1} SARS-CoV-2 IgG over a 20-day storage period at 4 °C (n = 3). Error bars in (a–d) represent the standard deviations of three measurements.

3.5. Ultrasensitive ECL detection of SARS-CoV-2 IgG antibody

Under the optimal experimental conditions, the proposed Bio-Ag/SA/Ru@bp-SNA/ITO sensor was used to detect various concentrations of SARS-CoV-2 IgG and the results were shown in Fig. 6a. A good linear correlation is found between the ECL intensity (I_{ECL}) and the logarithm of SARS-CoV-2 IgG concentration ($\log C_{IgG}$) from 5 pg mL^{-1} to 1 μg mL^{-1} ($I_{ECL} = -1453 \log C_{IgG} + 4646$ ($R^2 = 0.9966$)), which is superior to the commercial ELISA (6.25–200 ng mL^{-1}). The limit of detection (LOD) is determined as low as 2.9 pg mL^{-1} (S/N = 3), which is much lower than the concentration of the SARS-CoV-2 IgG in COVID-19 patient serum (20–40 μg mL^{-1}) and saliva (0.2–0.5 μg mL^{-1}) (Torrente-Rodriguez et al., 2020) and those previous reports (Table S1). Such excellent performance can be attributed to the high ECL intensity, good stability and high immunorecognition of SARS-CoV-2 spike protein. Total cost of our proposed Bio-Ag/SA/Ru@bp-SNA/ITO immunosensor for a single detection of SARS-CoV-2 IgG is about USD $1.29 (Table S2), which is compared with gold immunochromatography assay and ELISA (Table S3). Moreover, compared with ELISA (100–200 μL), the working volume of our immunosensor is only 50 μL of sample per measurement and even less by simply tailoring the electrode area. By comparison, our proposed sensor could simplify the operation steps (labeling and fabrication) and reduce the volume of samples and cost. However, our fabricated immunosensor could be inapplicable to strong alkaline solutions, which is resulted from the hydrolysis of bp-SNA.

The specificity, reproducibility and long-term stability of the developed sensor were also investigated. Except for SARS-CoV-2 IgG, the other five antibodies including anti-CEA, anti-PSA, anti-CA15-3, human total IgG and anti-SARS-CoV did not produce ECL responses at the Bio-Ag/SA/Ru@bp-SNA/ITO sensor (Fig. 6b). Even if these six antibodies were mixed, the ECL signal was basically consistent with that of a single SARS-CoV-2 IgG, indicating the excellent specificity of the immunosensor. Five Bio-Ag/SA/Ru@bp-SNA/ITO electrodes are prepared in parallel and their RSD for the detection of SARS-CoV-2 IgG (50 pg mL^{-1}) is 2.6%, suggesting the good reproducibility (Fig. 6c). The immunosensor displays stable responses over a 20-day storage period at 4 °C (Fig. 6d).

In addition, we studied the detection performance of the developed immunosensor in the practical application. As SARS-CoV-2 IgG is not detectable in the serum (healthy human) samples, standard addition method is employed. As shown in Table S4, human serum samples with artificially spiking in a defined amount of SARS-CoV-2 IgG were examined with satisfactory recoveries (between 96.3% and 105.0%). The RSD of three measurements ranges from 3.1% to 4.6%, exhibiting that the immunosensor is ultrasensitive, reliable, stable and low-cost.

4. Conclusions

In summary, we have developed an ultrasensitive and rather stable solid-state ECL platform for quantitative and reliable detection of SARS-CoV-2 IgG antibody by using bp-SNA as ECL luminophores nanocage. bp-SNA consisting of bilayer SNA with asymmetric surface charges can electrostatically confine the ECL luminophores ($Ru(bpy)_3^{2+}$) with high loading and stability, arising from the dual electrostatic force, namely electrostatic attraction by inner n-SNA and electrostatic repulsion by outer p-SNA. By modifying the recognized species, SARS-CoV-2 antigen, on the top surface of bp-SNA based on the biotin-SA binding reaction, the fabricated solid-state ECL immunosensor can realize ultrasensitive detection of SARS-CoV-2 IgG. The present ECL sensor is simple, economic and long-term stable, which paves a new way for the construction of solid-state probe sensors. Furthermore, more important biomolecules can be easily detected to meet the requirements for various analytical purposes, by facilely adjusting the recognitive ligands on the surface of bp-SNA.

Declaration of competing interest

The authors declare that they have no known competing financial interests or personal relationships that could have appeared to influence the work reported in this paper.

Acknowledgements

We gratefully acknowledge the valuable help with Prof. Wei Chen

and Dr. Wei Hu (School of Medicine, Zhejiang University, China) for providing anti-SARS-CoV-2 antibody and antigen. We acknowledge the financial support from the National Natural Science Foundation of China (21904117), the Zhejiang Provincial Natural Science Foundation of China (LY20B050007 and LY21B050003), and the Key Research and Development Program of Guangxi (AB18126033).

Appendix A. Supplementary data

Supplementary data to this article can be found online at https://doi.org/10.1016/j.bios.2022.114563.

References

Ali, M.A., Hu, C., Jahan, S., Yuan, B., Saleh, M.S., Ju, E., Gao, S.-J., Panat, R., 2021. Adv. Mater. 33, e2006647.
Bertoncello, P., Dennany, L., Forster, R.J., Unwin, P.R., 2007. Anal. Chem. 79, 7549–7553.
Collinson, M.M., Novak, B., Martin, S.A., Taussig, J.S., 2000. Anal. Chem. 72, 2914–2918.
Ding, H., Guo, W., Zhou, P., Su, B., 2020. Chem. Commun. 56, 8249–8252.
Etienne, M., Goux, A., Sibottier, E., Walcarius, A., 2009. J. Nanosci. Nano. Nanotechno. 9, 2398–2406.
Giordano, G., Vilà, N., Aubert, E., Ghanbaja, J., Walcarius, A., 2017. Electrochim. Acta 237, 227–236.
Goux, A., Etienne, M., Aubert, E., Lecomte, C., Ghanbaja, J., Walcarius, A., 2009. Chem. Mater. 21, 731–741.
Guo, W., Ding, H., Gu, C., Liu, Y., Jiang, X., Su, B., Shao, Y., 2018. J. Am. Chem. Soc. 140, 15904–15915.
Guo, Z., Dong, S., 2004. Anal. Chem. 76, 2683–2688.
Guo, Z., Shen, Y., Wang, M., Zhao, F., Dong, S., 2004. Anal. Chem. 76, 184–191.
Hu, L., Xu, G., 2010. Chem. Soc. Rev. 39, 3275–3304.
Khramov, A.N., Collinson, M.M., 2000. Anal. Chem. 72, 2943–2948.
Krammer, F., Simon, V., 2020. Science 368, 1060–1061.
Lee, C.Y., Lin, R.T.P., Renia, L., Ng, L.F.P., 2020. Front. Immunol. 11, 879.
Li, Q., Guan, X., Wu, P., Wang, X., Zhou, L., Tong, Y., Ren, R., Leung, K.S.M., Lau, E.H.Y., Wong, J.Y., Xing, X., Xiang, N., Wu, Y., Li, C., Chen, Q., Li, D., Liu, T., Zhao, J., Liu, M., Tu, W., Chen, C., Jin, L., Yang, R., Wang, Q., Zhou, S., Wang, R., Liu, H., Luo, Y., Liu, Y., Shao, G., Li, H., Tao, Z., Yang, Y., Deng, Z., Liu, B., Ma, Z., Zhang, Y., Shi, G., Lam, T.T.Y., Wu, J.T., Gao, G.F., Cowling, B.J., Yang, B., Leung, G.M., Feng, Z., 2020. N. Engl. J. Med. 382, 1199–1207.
Mi, X., Li, H., Tan, R., Tu, Y., 2020. Anal. Chem. 92, 14640–14647.
Miao, W., 2008. Chem. Rev. 108, 2506–2553.
Miller, C.J., McCord, P., Bard, A.J., 1991. Langmuir 7, 2781–2787.
Petherick, A., 2020. Lancet 395, 1101–1102.
Rashed, M.Z., Kopechek, J.A., Priddy, M.C., Hamorsky, K.T., Palmer, K.E., Mittal, N., Valdez, J., Flynn, J., Williams, S.J., 2021. Biosens. Bioelectron. 171, 112709.
Richter, M.M., 2004. Chem. Rev. 104, 3003–3036.
Sykora, M., Meyer, T.J., 1999. Chem. Mater. 11, 1186–1189.
Torrente-Rodriguez, R.M., Lukas, H., Tu, J., Min, J., Yang, Y., Xu, C., Rossiter, H.B., Gao, W., 2020. Matter 3, 1981–1998.
Walcarius, A., Sibottier, E., Etienne, M., Ghanbaja, J., 2007. Nat. Mater. 6, 602–608.
Wang, C., Horby, P.W., Hayden, F.G., Gao, G.F., 2020. Lancet 395, 470–473.
Wang, C., Zhang, N., Wei, D., Feng, R., Fan, D., Hu, L., Wei, Q., Ju, H., 2019. Biosens. Bioelectron. 142, 111521.
Wang, H., Xu, G., Dong, S., 2001. Analyst 126, 1095–1099.
Wei, H., Wang, E., 2008. TrAC, Trends Anal. Chem. 27, 447–459.
Wei, H., Zhou, L., Li, J., Liu, J., Wang, E., 2008. J. Colloid Interface Sci. 321, 310–314.
Woloshin, S., Patel, N., Kesselheim, A.S., 2020. N. Engl. J. Med. 383, e38.
Xiao, A.T., Tong, Y.X., Zhang, S., 2020. J. Med. Virol. 92, 1755–1756.
Yakoh, A., Pimpitak, U., Rengpipat, S., Hirankarn, N., Chailapakul, O., Chaiyo, S., 2021. Biosens. Bioelectron. 176, 112912.
Zhang, X., Bard, A.J., 1988. J. Phys. Chem. 92, 5566–5569.